TECHNISCHE MECHANIK
an open access journal

journal homepage: www.ovgu.de/techmech

Tech. Mech., Vol. 43, Is. 1, (2023), 189–202

Received: 31.01.2023
Accepted: 08.02.2023
Available online: 16.02.2023

CFD Assessment of an Ultralight Aircraft Including In-Flight Test Data Comparison

Gábor Zipszer[1]*, Bence Darázs[1], Ákos Horváth[1], Dávid Toma[1], Dániel Laki[1], Mátyás Gyöngyösi[1], Jenő Miklós Suda[2], Márton Koren[2], and Balázs Farkas[2]

[1] eCon Engineering Kft., H-1116 Budapest, Kondorosi út 3. 4.em., Hungary
[2] Department of Fluid Mechanics, Faculty of Mechanical Engineering, Budapest University of Technology and Economics (BME), H-1111 Budapest, Bertalan Lajos utca 4-6., Hungary

Abstract: In-flight test campaign was conducted with an ultralight aircraft to gather static and total pressure data over the aircraft surfaces and its surrounding using a purpose-built measurement system. The measured data served as the basis for the evaluation of the aircraft CFD simulation results. The CFD model considers the entire external geometry of the aircraft and utilises the in-house developed 3D corrected Virtual Blade Model to account for the propeller-induced flow field. The modelling approach and results are discussed and compared with the in-flight test data. A derivative of the baseline model was created with a detailed engine bay. The water and oil cooler devices were modelled with porous zones which properties were derived by explicit CFD simulation. The assessment of the flow field within the engine bay and the effect of the propeller-induced flow is discussed.

Keywords: virtual blade model, aircraft simulation, CFD, engine bay, in-flight measurement

1 Introduction

Enhancing internal Computational Fluid Dynamics (CFD) toolset is vital to meet the emerging needs and expectations of the general aviation industry. Currently, our focus is set on the propeller-driven small- and mid-sized aircraft, to develop methods being capable to account for the propeller induced flow field with higher accuracy utilising the virtual blade model described by Zipszer et al. (2022) and to apply it in steady-state calculations and in multi-objective optimisation tasks. The latter one usually requires fast, robust and accurate simulation methods enabling to perform dozens or even hundreds of simulations within a reasonable time.

Despite the aircraft's engine type – piston-engine or turboprop – the goal is identical: ensure adequate cooling of the engine bay under all circumstances and obtain low overall drag. To fulfil both at the same time, optimised cowls and cooling intake ducts are necessary. Depending on the aircraft design – tractor or pusher configuration, wing- or fuselage mounted engine(s) – the propeller could have a significant effect on cooling; thus, considering it in the models seems to be crucial.

The number of published studies on aircraft engine bay flow field and cooling analyses is limited, but started to increase recently. Balland et al. (2005) performed 3D CFD studies in the nacelle core compartment of an aircraft gas turbine engine and compared the results with real engine data. Since 2013 many papers have been published related to the European project called ESPOSA. Many of them, like Lapka et al. (2014), Lapka et al. (2018) and Gula et al. (2019) focus on the thermal analysis of the I 23 aircraft's engine bay, in which the piston-engine was replaced by a TP100 turboprop engine. Stalewski and Zóltak (2014) interpret CFD models using virtual blade model (VBM) based on blade element theory (probably without correction of 3D effects), together with parametric shape optimisation method of the engine intake duct and the cowl. Under the same ESPOSA project Buonomo et al. (2013) presented the CFD thermal analyses of EM-11 ORKA aircraft's engine nacelle, both considering external and internal flows, but in a separated manner. Olejnik et al. (2021) describes the detailed CFD analyses of OSA aircraft in pusher configuration both modelling external and internal engine bay flows in the same model utilising an actuator disc with constant pressure jump as substitution of the propeller.

Multiple goals were set for the current research:

1. Validation of the applied CFD method on an aircraft at gliding conditions by comparing results with in-flight test data.
2. Validation of the in-house developed 3D corrected virtual blade model (3D-VBM) described by Zipszer et al. (2022) in the CFD model of the same aircraft by comparing results with in-flight test data.
3. Assessment of the propeller wash effect on engine bay flow rates and to derive a simplified engine bay model.

To achieve these goals a purpose-built in-flight data acquisition system was developed and flight testing were conducted. Also, an engine bay and an external aero CFD model of the entire aircraft were created with the implementation of the in-house 3D-VBM.

The utilised aircraft was a motor-glider with piston-engine, tractor configuration, called Altus Concept (HA-XDK). It is depicted in Fig. 1.

* E-mail address: gabor.zipszer@econengineering.com doi: 10.24352/UB.OVGU-2023-055

Fig. 1: Altus Concept ultralight motor-glider

2 In-Flight Measurement System

The simplified schematic of the data acquisition system (DAQ) is presented in Figure 2. The pressure signal is transmitted via PTFE pneumatic lines from the probes to the transducers. The pressure signals are converted to electric signals by Honeywell TruStability HSC series analogue pressure transducers. The data acquisition is performed by two National Instruments NIUSB-6002 providing 16 parallel analogue channels. The acquired data was stored on a portable personal computer trough which the operator also could control the measurement sequence and monitor the instantaneous measurement results in-flight. The frequency resolution of the DAQ was initially expected to be within the range defined by the blade passing frequency (BPF). The DAQ can acquire data at 6.25 *kS/s* rate, which is adequate within the frequency range of 0-3 *kHz*. A part of the measurement chain was investigated separately to validate if the required frequency resolution was achieved. In order to define the frequency response of the system, the pressure tap was placed into an acoustic enclosure. It was excited by a continuous pressure signal provided by a wide frequency range speaker with monotone increased frequency in time in accordance with the work of Jackson and Vinegar (1979). The obtained signal from the transducer was compared to the undisturbed pressure signal which was provided by a precision Endevco 8507C-1 type pressure sensor with 55 *kHz* cut-off frequency. The resulted frequency response curves are plotted in Figure 3 in the case of three different pneumatic line lengths. The lengths of the line sections were defined based on the 3D CAD model of the airframe before the installation of the system on the aircraft. It can be observed that adequate readings can be performed up to 350 *Hz* if the 1.4 *m* long PTFE lines are used.

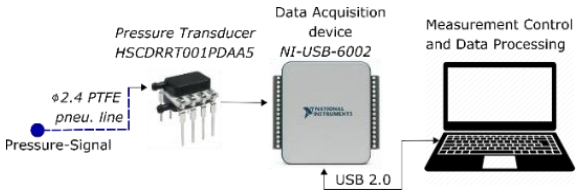

Fig. 2: Schematic of the data acquisition system

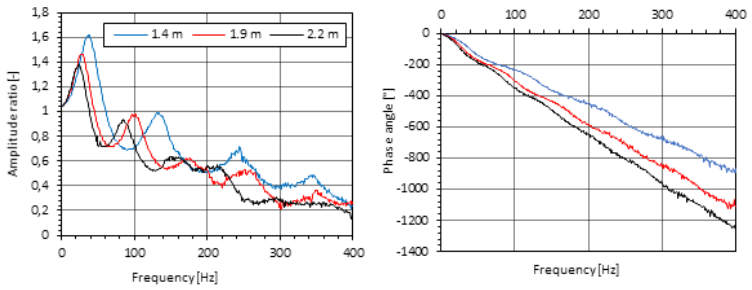

Fig. 3: Frequency response curves for different tube lengths

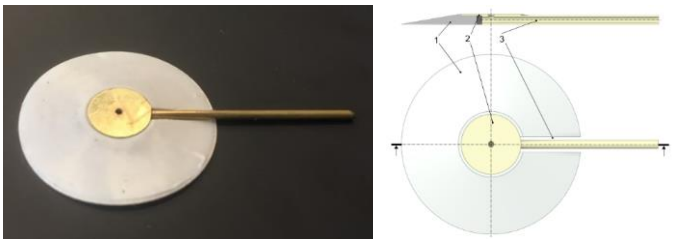

Fig. 4: Isolated static pressure probe

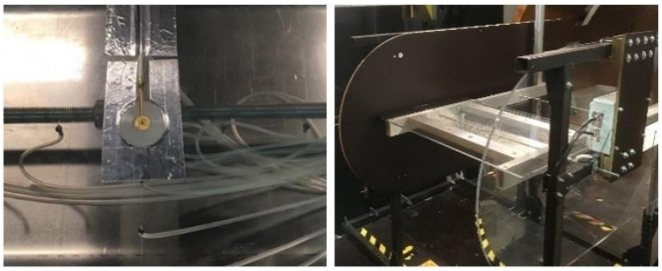

Fig. 5: Isolated static pressure probe on the test device

2.1 Pressure Probes

Within the measurement campaign, three different types of pressure probes were used. The reference dynamic and static pressures were measured by a KIMO-TPL-06-800 type Pitot-static probe. During the measurements, the probe was positioned 1 *m* upfront the wing leading edge using a composite boom to provide pressure readings outside the disturbed flow-field by the airframe. The position of the probe was confirmed by preliminary CFD computations.
The total pressure distribution around the airframe was measured by Evolution-Vectoflow Kiel probes. The probes are manufactured by 3D metal printing and provide an accurate reading within the range of ±60° angle of attack (AoA), which was confirmed by wind tunnel measurements.
The surface static pressure distribution on the airframe was measured by coin type isolated static pressure probes (ISPP) based on the work of Pelley et al. (2012) because the airframe itself could not be modified for the purpose of the measurements. It practically meant that the pressure taps could not be mounted flush to the skin of the airframe. Therefore, pressure taps had to be developed which could be mounted to the surface by adhesive. The ISPP can be seen in Fig. 4. The tap is built up of three major parts: the moulded silicon fairing (No.1 in Fig. 4.), the copper disc with the pressure tap orifice (No.2 in Fig. 4), and a Ø1.0xØ1.5 *mm* copper tube (No.3 in Fig. 4). The copper tube and the disc are soldered together and are connected to the fairing by an instant adhesive system. The overall height of the pressure tap assembly is 1.74 *mm*, the outer diameter of the fairing is 30 *mm*, and the diameter of the copper disc is 10 *mm*.
As a result, these ISPP's can be used on almost any surface of the airframe, i.e. they can be easily attached or removed. Although it's practical benefits, this pressure tap needs to be calibrated. Since the pressure tap sticks out from the surface, the measured pressure (p_{M}) is expected to be lower than the true pressure (p_{R}) above the surface of the skin of the airplane as it is discussed in the work of Mackay (1990). The deviation or *error* caused by the pressure tap was assessed experimentally. The flat plate mounted pressure tap and the wind tunnel test setup is depicted on Figure 5. The measurement system was tested and calibrated in the wind tunnel of the Theodore von Kármán Wind Tunnel Laboratory at BME. Further reference about the wind tunnel can be found in the work of Balczó et al. (2006). The horizontally aligned flat plate in Figure 5 is mounted between two endplates to keep the airflow parallel as the AoA changes. The width of the flat plate is 1 *m* and the length is 0.66 *m* and was equipped with 20 flush mounted pressure tap orifices placed evenly along the longitudinal and lateral midlines. The pressure tap was positioned in the middle of the flat plate and the p_{M} results were compared to the pressure measured on the empty plate (p_{R}). The tests were carried out at wind velocities varied between 15–45 *m/s* and AoA's varied from –20° to +10° where positive means leading edge down. The test results are presented in Fig. 6. At positive AoA's, the difference between p_{R} and p_{M} is low as the isolated pressure tap does not protrude from the thickened boundary layer. At negative AoA's, the difference increases significantly and reaches up to 14% of the dynamic pressure.
Based on the experimental results the measured pressures can be compensated by using Eq. 1 to reduce the discrepancy between the measured and real pressure.

$$p_{\mathrm{M,comp}} = p_{\mathrm{M}} + K_0 p_{\mathrm{dyn}} \tag{1}$$

Beside the region presented in Fig. 7 the difference between the measured and real pressure (*error*) as function of p_{dyn} and p_{M} is not monotone, i.e. more than one error value can be assigned to a given pair of p_{dyn} and p_{M}. Therefore, the definition of the compensation coefficient (K_0) requires further consideration to be taken into account.
In case p_{M} and p_{dyn} fall in the region presented in Fig. 7 the measured static pressures (p_{M}) can be compensated directly with the measured *error* values.
If the pressure tap is installed into an area where the flow is separated, the results do not have to be compensated since the

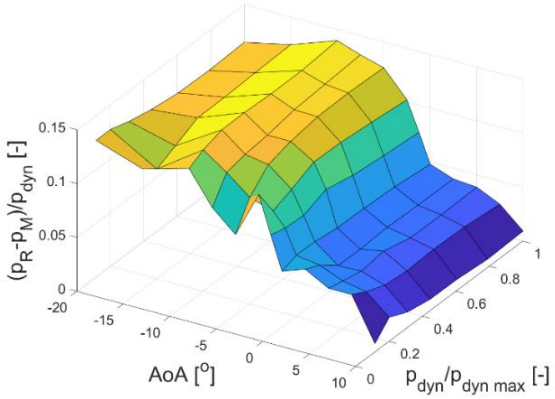

Fig. 6: Relative difference between p_{M} and p_{R} as function of the measured p_{dyn} and the AoA

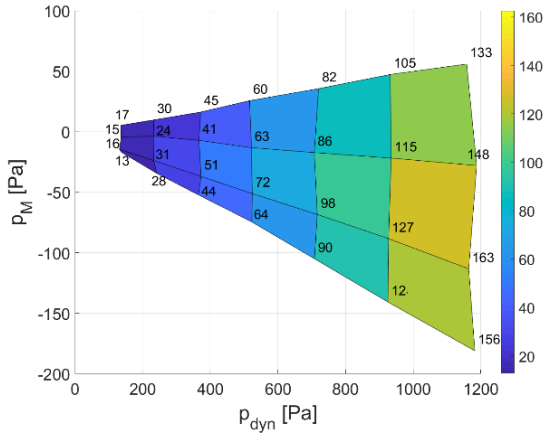

Fig. 7: Difference between p_{M} and p_{R} (*error*) as function of p_{dyn} and p_{M} in the region where direct compensation can be applied

error in this case is expected to be small. The occurrence of flow separation can be confirmed by flow visualisation, e.g. by applying wool tufts.
In areas of not fully developed separation or within the bordering region between separated and non separated regions the $K_0 = 0.05$ constant can be applied.
If the given pressure tap is installed into a place, which fell out from the regions described above, then two correction coefficients, $K_{0,\mathrm{H}} = 0.1064$ and $K_{0,\mathrm{L}} = 0.0613$ can be applied. In this case, one of the two compensated pressures ($p_{\mathrm{M,comp}}$) will fall within the ±30 *Pa* range of the real pressure (p_{R}). However, based on only two measured properties, p_{dyn} and p_{M}, it cannot be determined which compensated pressure is the valid one. If compensation is not applied, then the maximum *error* can reach up to 120 *Pa* within the investigated range.

3 CFD Models

The CFD modelling approach consisted of two steps:

1. Building and simulating the engine bay internal flow with a portion of the external flow only, together with propeller induced flow effect using the 2D-VBM. The main goal was to determine flow rates through engine cowl openings at different flight conditions.
2. Building and simulating the external aero model of the full aircraft using 3D-VBM with derived engine bay inlet/outlet flow rates.

For both models Ansys Fluent v2020R2 finite volume code was used applying Reynolds-averaged Navier Stokes method in steady-state time frame, together with k-ω SST turbulence model. The solver applied was the pressure based pseudo-transient coupled solver of Fluent, in all cases with second order scheme for pressure and momentum, and first order upwind scheme for turbulence equations.
The working medium was always air at constant density and viscosity at 15°*C*, with operation pressure of 101325 *Pa* (Sea level ISA condition).

3.1 Engine Bay Model

The engine bay CFD model is depicted in Fig. 8. It is a rectangular domain with the aircraft positioned at its second half on the centreline. The aircraft tail and the outer sections of the wings were outside this domain, as they have negligible influence on the flow inside the engine bay. The model is based on the 3D CAD model of the aircraft and parts inside the engine bay.

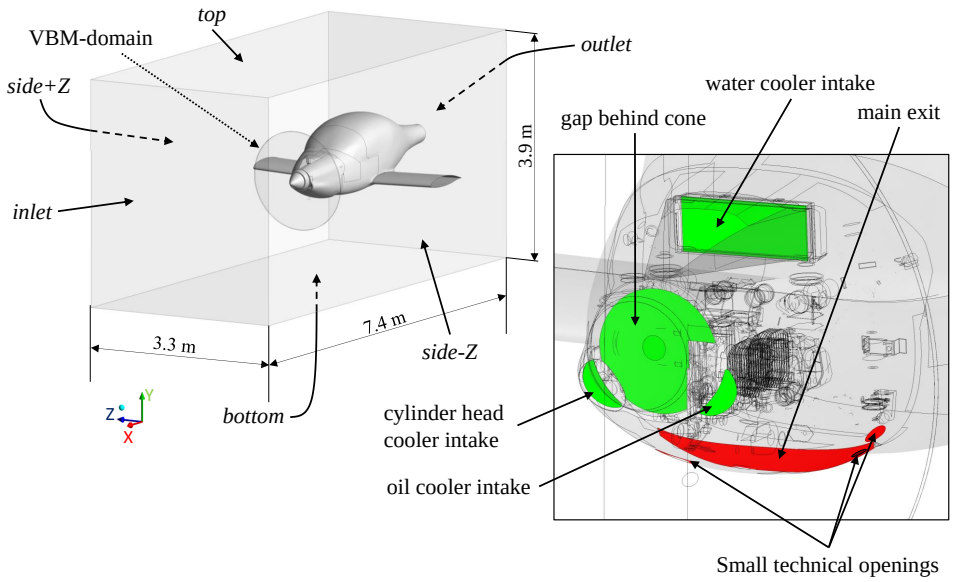

Fig. 8: Engine bay CFD model overview

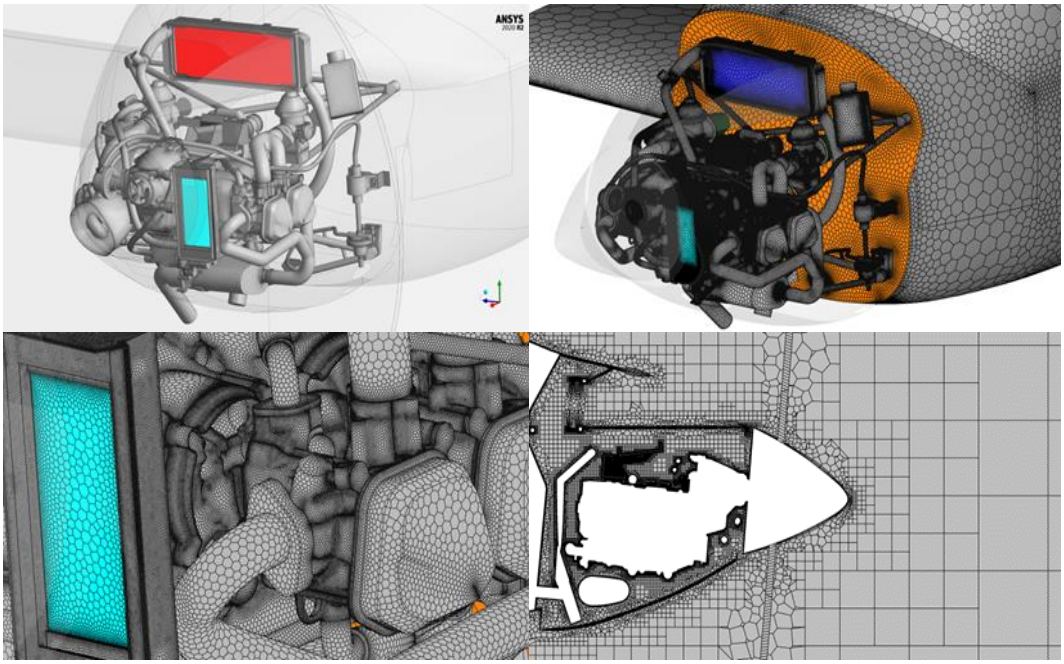

Fig. 9: Details of the engine bay CFD model

The intakes and exits are depicted in Fig. 8 by green and red surfaces, respectively. The CAD model was cleaned in Ansys SpaceClaim. Very small, tight gaps were filled-in to decrease cell count and increase mesh quality, but the smallest modelled feature is still in the range of few millimetres. The propeller was substituted using a 1626 mm diameter one-cell thick (20 mm) VBM disc constructed from structured hexahedral elements.

The water and oil coolers were substituted with equivalent porous media, which parameters were determined in separate pre-studies. For that purpose, representative section of each cooler was isolated and simulated to obtain pressure loss characteristics and viscous and inertial resistance parameters. It was assumed that these parameters are 1000 times larger in transverse than in streamwise direction. Applying this assumption improves convergence performance, but still restricts the transverse flow.

Usually, for such complex CAD models the fault tolerant meshing workflow (wrapping) is adequate and straightforward to apply, but it could trim features of interest, therefore, the so-called watertight meshing workflow was used instead. The surface mesh minimum and maximum cell sizes were 0.8 mm and 200 mm, respectively. The volume mesh was poly-hexcore type with 3 boundary layers at walls, both at internal and external surfaces. This resolution at equivalent airspeed (EAS) 122 km/h flight speed results in $y^+ \approx 8$ at engine bay internal surfaces, $y^+ \approx 60$ at engine cowl outer surface, and $y^+ \approx 200$ at wings and fuselage. The resulting final mesh consisted of 51.7 million nodes and 15.4 million cells. The CAD model, surface mesh on engine bay internals and the volume mesh in a cross-section view are shown in Fig. 9.

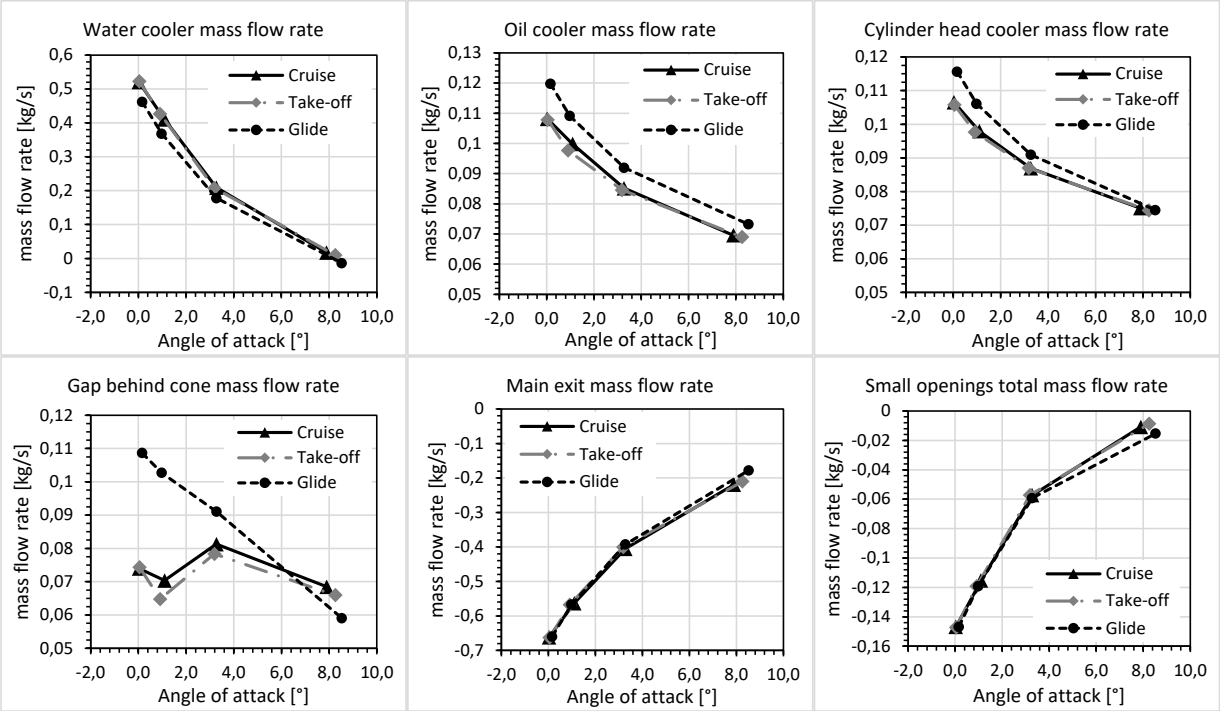

Fig. 10: Mass flow rates through engine bay openings

The following boundary conditions were applied:

1. *Inlet*, *side-Z*, *side+Z*, *top* and *bottom* surfaces: velocity inlet with x- and y-component according to AoA and flight speed. The turbulent intensity and viscosity ratio were set to 1% and 1, respectively.
2. *Outlet* surface: pressure outlet with 0 Pa average gauge pressure.
3. *Engine intake filters* (left and right): mass flow rate outlet boundary condition with 0.03762 kg/s, each, independently of flight speed.
4. *Exhaust gas pipe*: mass flow inlet with 0.080232 kg/s (fuel + air mass flow rate).
5. All physical walls were defined as hydraulically smooth *wall* with no slip boundary condition.

The VBM applied in these simulations was the 2D-VBM specified in Zipszer et al. (2022), since at the time of these simulations the 3D correction method was not finalised yet. However, the 2D-VBM was considered sufficient for our purposes since the engine cowl openings are located at lower diameters where 3D effects are expected to be less influential. VBM inputs were given as specified in Zipszer et al. (2022).
In total 12 cases were simulated: cruise, take-off and gliding conditions, each at 4 different flight speeds ranging from EAS 94.7 km/h to 169.6 km/h. The AoA ranged from ≈0° to ≈8.5°, accordingly. The difference between cruise and take-off conditions was the propeller blade pitch with a difference of 3.8°. In glide the VBM was switched off.
The simulations ran until convergence of residuals and monitored flow rates (usually around 50 iterations), and afterwards for additional 500 iterations with *steady statistics* option switched on to obtain iteration-averaged flow field and quantities. Stronger oscillations were observed at higher AoA, particularly in water cooler inlet flow rate.

3.2 Engine Bay Results

During postprocessing the focus was on the mass flow rates through the engine bay openings. In Fig. 10 the calculated mass flow rates through the intakes (water cooler, oil cooler, cylinder head cooler and gap behind cone) are depicted in function of AoA for the three flight conditions. As it can be seen, at take-off and cruise conditions the mass flow rates are very similar. In gliding they are a bit different, particularly through the gap behind the cone (propeller spinner).
At low AoA (<2°) the flow rate through the water cooler is the largest, but decreases fast with increasing AoA, and it becomes ≈0 kg/s at AoA≈8°. This is in line with experience: on hot days climbing can be limited due to excessive coolant temperature. The running propeller increases the flow rate by 12-18%, but at high AoA it can barely compensate the losses.
The mass flow rates through the oil cooler and cylinder head cooler intake ducts are very similar, particularly at glide condition (±2%). Both are much less sensitive to AoA compared to the water cooler, and interestingly the propeller wash decreases their flow rate by 6-10%.
The mass flow rate through the gap behind the propeller cone in glide is similar to that of the oil- or cylinder head cooler, but in cruise and take-off it shows a constant behaviour with a value of 0.073 kg/s and 0.07 kg/s, respectively.
The hot air can exit the engine bay either through its main exit face or through any of the small technical openings (ring face around exhaust pipe and two technical holes). One can observe that 82-95% of the total flow exits through the main exit, with larger portions at higher AoA. The propeller wash barely affects this ratio.

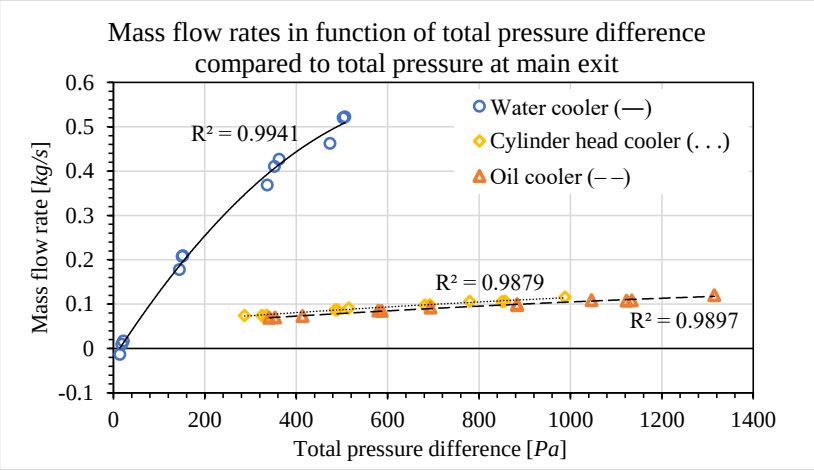

Fig. 11: Mass flow rates through engine bay intakes in function of total pressure difference

In order to be able to run intake shape optimisation studies accounting for engine bay flow, it seems necessary to use some simplified methods to model the engine bay intake/exit flows. For that purpose, the area averaged total pressures were derived at intake surfaces, as well as at the main exit. The mass flow rates through the intakes are shown in function of the calculated total pressure differences (intake-exit) in Fig. 11 for the water-, oil- and cylinder head cooler intakes. As can be noted the fitted 2nd order polynomial trendlines agree well with the explicit results, at least in the range of our current interest. The oil- and cylinder head coolers follow very similar trends, as expected from their nearly symmetric arrangement and size. The trendline of the water cooler also fits nicely at both low and high total pressure differences.
In conclusion, the method to define mass flow rates through intakes based on the total pressure differences using the determined characteristics seems reasonable. However, in our full external aero model, which is described in the next chapter, the inlet and outlet flow rates were defined explicitly as the same operating conditions were applied.

3.3 External Aero Model

The CFD domain used for the external flow simulations is depicted in Fig. 12. It is a cylindrical domain (Ø100 m) with a hemisphere inlet face at its front. The model is based on the 3D CAD model of the aircraft. In the CFD model the three main air intakes (water-, oil- and cylinder head cooler) and the engine bay main exit were considered as it shown in Fig. 12. The propeller was substituted with the same VBM disc domain as in the engine bay model.
The final volume mesh was poly-hexcore type with prism layers at the walls. The minimum and maximum cell length were 5 mm and 1.2 m, respectively. The finalised baseline mesh featured 17 prism layers resulting in $y^+ \approx 20$ at 47.1 m/s free-stream velocity with local maximum y^+ values of 30. The mesh of the VBM domain was the same as in the engine bay model. Cross section views of the finalised baseline volume mesh (36.7 million nodes, 17 million cells) are shown in Fig. 13.
The following boundary conditions were applied:

1. *Inlet* and *side* surfaces: velocity inlet with x- and y-component according to AoA and flight speed. The AoA was tuned in each case to achieve a lift force matching the total weight of the aircraft within 1%. The turbulent intensity and viscosity ratio were set to 1% and 1, respectively.
2. *Outlet* surface: pressure outlet with 0 Pa average gauge pressure.
3. *Water*-, *oil*- and *cylinder head cooler intakes* and *main exit outlet*: mass flow outlets and inlet with specified mass flow rates derived from detailed engine bay simulations.
4. All physical walls were defined as hydraulically smooth *wall* with no slip boundary condition.

The applied VBM model details are specified in Zipszer et al. (2022). The same inputs were used for the 2D- and 3D-VBM; identical to the 2D-VBM inputs used in the engine bay simulations.

3.4 Mesh Sensitivity Study

The mesh sensitivity study was carried out in two steps. The aim of the first study was to find that inflation-layer and surface mesh setting combination which provides sufficient mesh density and good mesh quality, while keeping the final cell count within a manageable range, which should not be more than 45 million in our case. Our target of maximum y^+ value at the maximum flight speed was 30, therefore the inflation layer was set up accordingly. This initial sensitivity study was carried out on a separate model consisting of a 1 m segment of the aircraft inboard wing, where its profile was constant. Several parameters, such as maximum and minimum surface mesh sizes, curvature angles and growth rates, and inflation-layer settings were varied and their effect on generated lift was investigated. In our case the effect on drag was not considered as accurate drag prediction was out of scope for the current project.
Based on the data collected during the inflation-layer parameter study, the absolute thickness was found to be one of the most critical parameters. In our case the maximum thickness was not a direct, explicit parameter, but it depended on the other

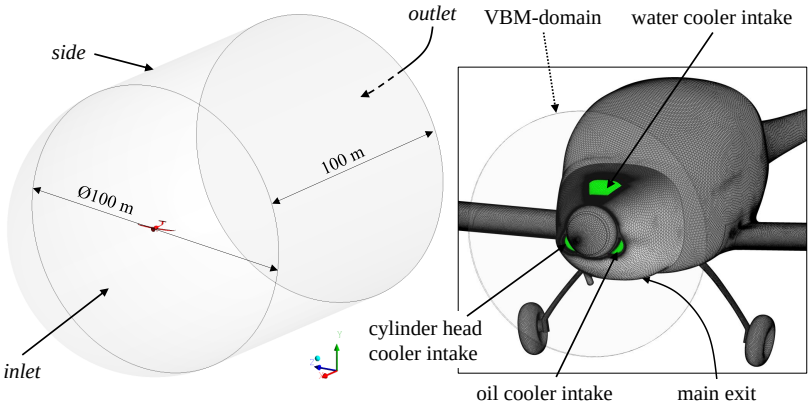

Fig. 12: External aero CFD model layout

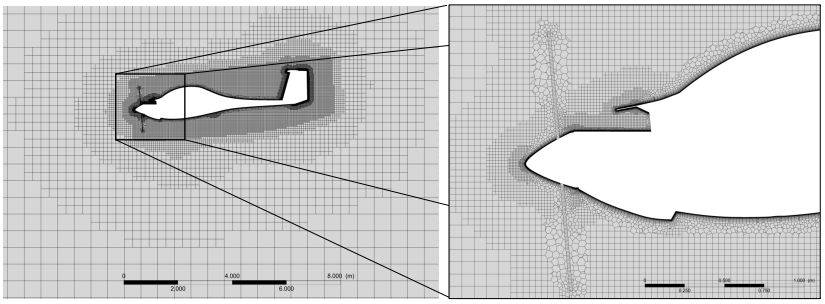

Fig. 13: Finalised baseline volume mesh

inflation-layer settings, such as first cell height, number of layers and growth rate. By plotting the lift force values generated by the wing segment under consideration in function of the thickness of the inflation-layer a sudden change was observed around 10 mm of inflation-layer thickness. This trend is shown in Fig. 14. After the detailed investigation of the flow field around the wing segment for the different inflation-layer settings it was found, that by further decreasing the inflation-layer once the inflation-layer thickness reached the thickness of the calculated turbulent boundary layer, it affects adversary the derived turbulent boundary layer. The thinner inflation-layer artificially compresses the turbulent boundary layer. Our hypothesis is, that by artificially compressing the turbulent boundary layer, the derived flow field will separate further away from the wing trailing edge, hence reducing its lift generation capabilities.

Additional finding of the initial mesh sensitivity study was that by keeping a desired value of transition ratio between the inflation-layer last element and the volume mesh, there will be a critical surface mesh size upon which further increasing it the overall volume cell count will not decrease. This is due to the fact, that the inflation layer will require an increased number of layers to maintain the target transition ratio. In our case this limiting surface cell size found to be around 20 mm. The trend of the volume cell number variation with maximum surface cell size is depicted in Fig. 15. The finalised baseline mesh settings are summarised in Tab. 1 which were used within the Watertight Geometry Workflow of Ansys Fluent Mesher.

The second mesh sensitivity study was focusing on the effect of lowering the target maximum y^+ value over the wing and fuselage from 30 down to 5 and then down to 1, while keeping the surface mesh settings fixed. This study was carried out on the full external aero CFD model using two cases of the actual flight test campaign focusing on the monitor points which are representing the static pressure probes positioned over the wing upper surface out of the effect of the propeller slip stream. These monitor points were labelled from SZ1 to SZ5 and are depicted in Fig. 16. The inflation-layer parameters for the three different types are summarised in Tab. 2. In Ansys Fluent Mesher the so called Last-Transition type inflation-layer was used as it allowed a direct control over the first cell height – so the y^+ value – and the transition ratio.

The relative static pressure – the difference between the absolute static pressure at the monitor point and the ambient absolute static pressure – was derived for the monitor points SZ1-SZ5 at two different flight cases for the second mesh sensitivity study. These flight cases were VT100m2 and VT130m2, where VT stands for glide operation (stabilised descend without operating engine and propeller) at target True Air Speed (TAS) of 100 km/h and 130 km/h, respectively. The m2 label indicates that this case was derived based on the averaged dynamic pressure data from the second measurement campaign. The calculated relative static pressures at the monitor points of SZ1-SZ5 for flight case VT100m2 and VT130m2 are plotted in Fig. 17 left-side and right-side, respectively. As these static pressure taps were mounted on the wing upper surface consecutively with similar distances from each other, we use line and point-plot style graphical representation. Please note, that the y^+=30 values are plotted with dashed-line, while the other datasets with rectangle and plus-sign without lines. The average of relative pressure changes between y^+=30 and y^+=5 was 2.9 Pa, while between y^+=5 and y^+=1 it was only 0.4 Pa. After the evaluation of the calculated data one can conclude, that there was no significant change in the relative static pressure values, therefore the inflation-layer with the current surface mesh settings and with the applied solver settings and turbulence model is sufficiently resolved.

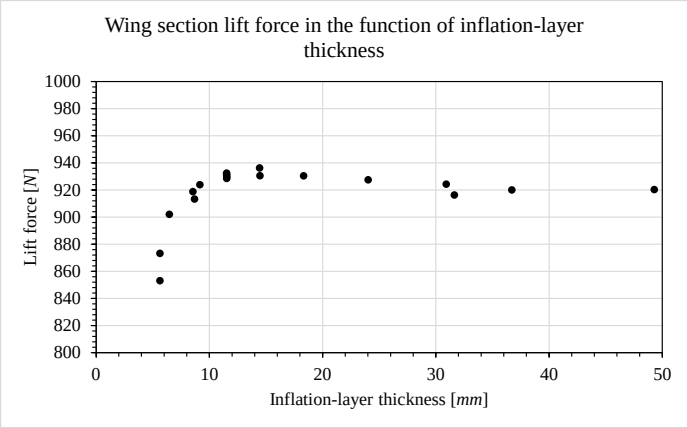

Fig. 14: Variation of lift force with inflation-layer thickness

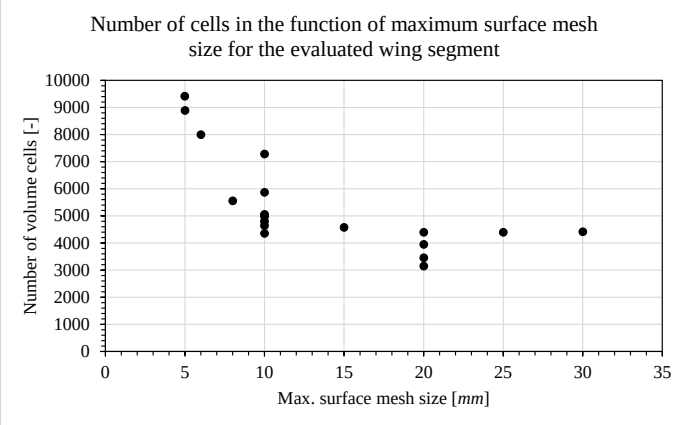

Fig. 15: Variation of volume cell count with maximum surface mesh size

3.5 External Aero CFD Result Assessment

The simulated cases were stabilised glide with non-operating engine (VT) and stabilised level flight with cruise (CR) or take-off (TO) blade pitch settings. For each setting there were four flight speeds (TAS 100, 130, 160 and 180 km/h) where the measurement took place. The results and test data derived for cruise and take-off blade settings showed very similar trends as the blade angle varied only by approx. 3.5 deg and the propeller speed of rotation (rpm) was set to maintain the same flight speed, therefore producing the same thrust. The reason for measuring at these two different blade pitch settings was, that these were the most closed and most open settings, also the actual effect of such blade angle change on the induced flow field was initially unknown.
In the CFD model monitor points were defined based on the physical location of the pressure probes. The probe locations were selected based on initial CFD studies. The actual position of the probes was determined by manual measurements after the probes were installed onto the aircraft. These locations then were replicated in the CAD model so their coordinates could be derived and used in the CFD model to position the monitor points.
Please note that for data comparison corrected measurement data were used and depicted in the figures within this document. The applied correction factors were derived based on qualitative assessment of the flow field supported by CFD simulation and the behaviour of wool tufts applied onto the aircraft surfaces and were monitored by external cameras. The correction factors are discussed in section 2.1 above.

3.5.1 Angle of Attack Setting Procedure

During the in-flight test campaign, the ambient static and total pressures were measured by the Pitot static probe mounted on the aircraft wing such that it had no interference with the aircraft and the dynamic pressure could be directly determined. Using this dynamic pressure and assuming SL/ISA conditions (sea-level, standard atmosphere) the velocity magnitude was derived for the applied velocity-inlet boundary condition. On the other hand, the aircraft had no AoA measurement device, therefore the velocity components could not be directly derived. However, the correct AoA setting is very important when one attempts to compare in-flight measurement data with CFD simulation results. To be able to resolve this problem the total mass of the aircraft including fuel and crew were monitored and controlled during the test campaign. Knowing the total mass, the weight could be derived. The inflow velocity components at the inlet boundary were tuned manually until the lift force calculated by the CFD model matched the actual weight of the aircraft.
It must be noted, that the derivation of lift force is different for constant level-flight cases – when the propeller is in operation, and the aircraft can maintain its altitude and speed – compared to stabilised descent, or glide, when the engine is switched

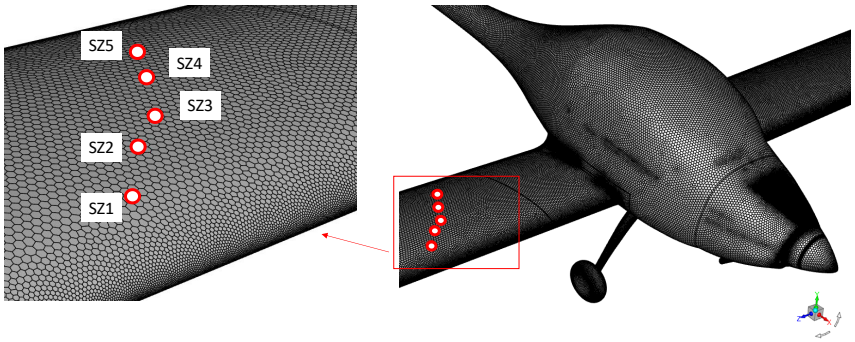

Fig. 16: Surface mesh of the aircraft and its wing with the monitor points SZ1 to SZ5

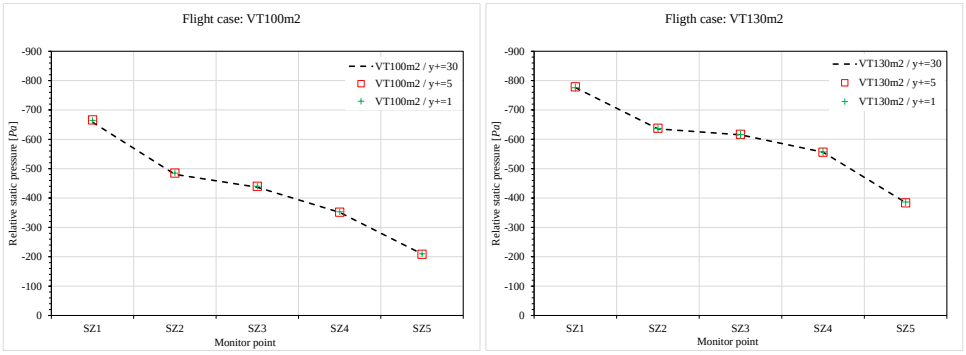

Fig. 17: Calculated relative static pressures at monitor points SZ1 to SZ5 for different inflation-layer settings

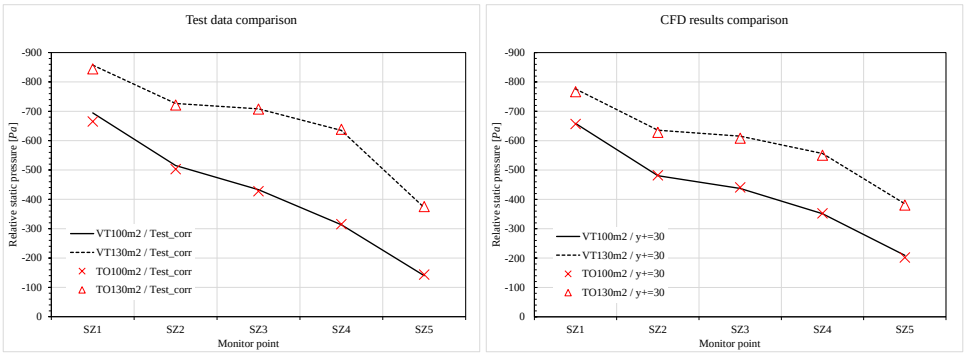

Fig. 18: Relative static pressures of SZ1 to SZ5 at different flight cases: measurement data (left) and CFD results (right)

off, therefore the aircraft cannot maintain its speed and altitude at the same time. For constant level flight the lift force must compensate the aircraft weight force. While for stabilised descent the resultant aerodynamic force – the vectorial sum of lift and drag forces – acts against the aircraft weight.

This AoA setting procedure can be checked by evaluating the measured and predicted relative static pressures for probes SZ1 to SZ5. The position of these probes can be seen in Fig. 16. Fig. 18 shows the relative static pressures of the probes or monitor points from SZ1 to SZ5 at different flight cases. Please note, that VT values are plotted with lines, while TO data is plotted with markers only. It can be seen, that pressures for VT100m2 and TO100m2 flight cases are aligned for the measured data and for the CFD prediction, as well as for VT130m2 and TO130m2 flight cases. Two conclusions can be made from these graphs. One is that SZ1-SZ5 probes were not affected by the propeller induced flow field because there is no significant difference between VT and TO cases neither in test data nor in the CFD results. This is in line with expectations.

The other conclusion is that the AoA setting procedure is correct in terms of using different approach for glide and level flight cases; if that was not the case then there would be a different trend in matching VT and TO pressures either for measurement or CFD simulation.

3.5.2 VBM Blade Pitch Setting Procedure

In order to set up the VBM model correctly the actual propeller rpm and the blade pitch angle need to be known. The motor rpm was recorded for each flight case. Knowing the gearbox ratio, the actual propeller rpm could be directly derived. As we used SL/ISA ambient conditions during the CFD simulations we had to scale the propeller rpm from actual to SL/ISA equivalent to ensure that we maintain the same propeller advanced ratio which is defined as $J = V/nD$, where V is flight velocity, $n = rpm/60$ is the speed of rotation and D is the propeller diameter. To be able to do the scaling we needed to know the true air speed of the aircraft, which was derived from the measured dynamic pressure and air density. Air density was derived based on the ambient static pressure and temperature at the airfield and flight altitude.

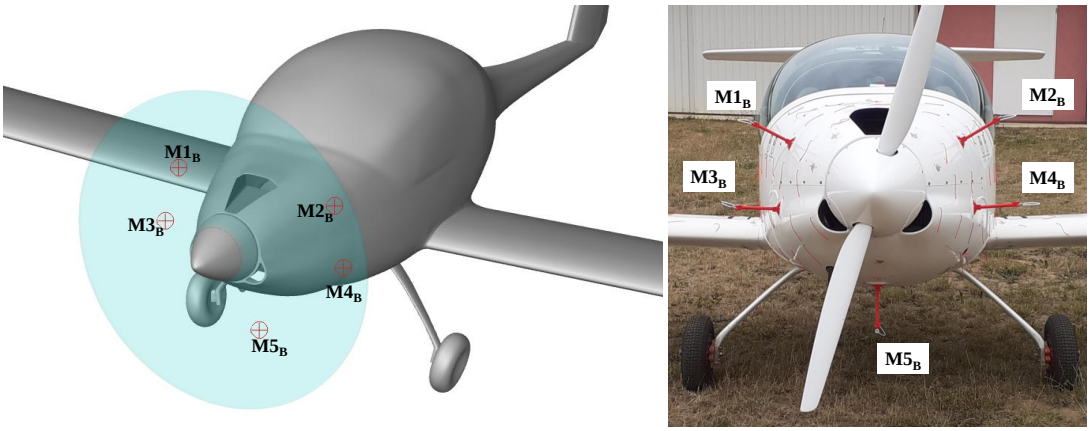

Fig. 19: Location of monitor points and Kiel pressure probes $M1_B$ - $M5_B$

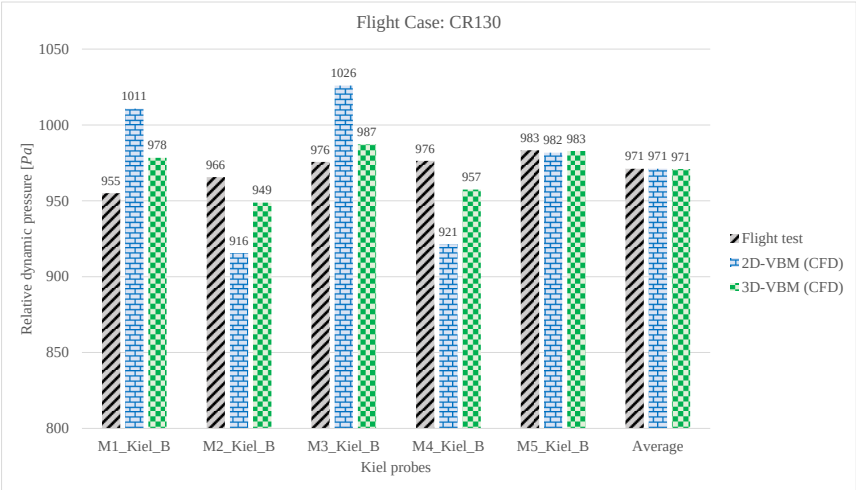

Fig. 20: Variation of relative total pressures behind the propeller

This VBM tuning was carried out for all cases with the VBM in operation parallel with the AoA tuning. The Kiel probes and corresponding monitor points used for VBM tuning are depicted in Fig. 19. The variation of measured relative total pressures behind the propeller and the CFD results at the corresponding monitor points for 2D-VBM (conventional, uncorrected) and for 3D-VBM are shown in Fig. 20. It can be seen, that the averaged relative total pressures matched with measurements. The individual relative total pressures predicted by the conventional 2D-VBM shows significant deviations compared to actual measurements with an averaged deviation of 43 Pa which is 4.43% of the averaged value. The 3D-VBM shows noticeable improvement compared to the 2D-VBM solution with an average deviation of 14 Pa which is 1.44% of the averaged value. A similar trend can be observed for the other cases with the VBM in operation which leads to the conclusion that the 3D-VBM provides a noticeably better match to the in-flight test data, which can be a significant factor when the CFD model is used for the evaluation of propeller-airframe interaction or airframe shape optimisation in the vicinity of the propeller.

3.5.3 Comparing CFD Results with Test Data

If we compare the static pressure coefficients (c_p) from the test– which is relative static pressure divided by the free-stream dynamic pressure – of the aforementioned probes from SZ1 to SZ5 with the CFD results we can see that the trends are captured relatively well as it is depicted in Fig. 21. However, there are notable differences in the c_p values between measurement and CFD. For TO100m2 CFD underpredicts measurement for SZ1 and SZ2 by Δc_p of 0.058 (3.3%) and 0.083 (6.1%), it ties up with measurement at SZ3 (difference of 1%) and overpredicts measurement at SZ4 and SZ5 by Δc_p of 0.079 (9.5%) and 0.143 (37.6%). For the other cases a relatively even underprediction of c_p can be seen with a maximum deviation of 0.188 (31%) for SZ4 at TO180m2; the average is 0.123 (13.1%). This even shift between measurement and CFD results for cases excluding TO100m2 might indicate that another calibration factor should have been applied – which has not been derived during the calibration of the data acquisition system. It must be noted, that the calibration of the isolated static pressure probes (ISPP) was carried out using a flat plate. Probably, further calibration factors could have been derived for airfoil profiles.
The standard deviation of measured static pressure coefficient (c_p STD) is depicted in Fig. 22. For most cases the c_p STD are below 0.019 except case TO160m2 which has a maximum c_p STD of 0.027; it is still less than 3% of the actual c_p of -0.9107.
Another five monitor points will be discussed, which are depicted in Fig. 23. M1 and M5 are static pressure probes on the motor cowling surface. $M1_B$ is a total pressure probe near the cowling. SZT1 and $SZT1_A1$ are static and total pressure probes, respectively, located near to the rear side of the wing-fuselage transition where significant pressure fluctuations were expected to occur. Both total pressure probes were positioned ≈20 cm from the airframe surface.

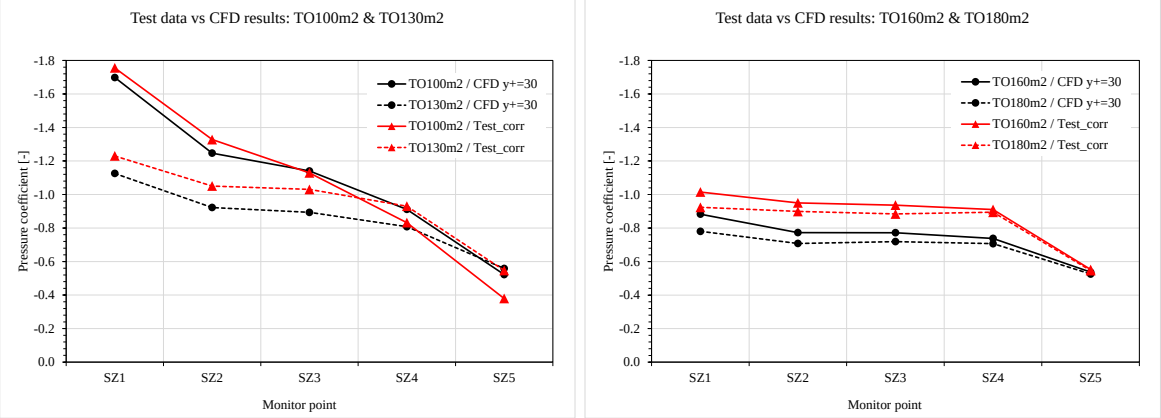

Fig. 21: Comparing measured and calculated static pressure coefficients of SZ1 to SZ5 for different flight cases: TO100m2 and TO130m2 (left), TO160m2 and TO180m2 (right)

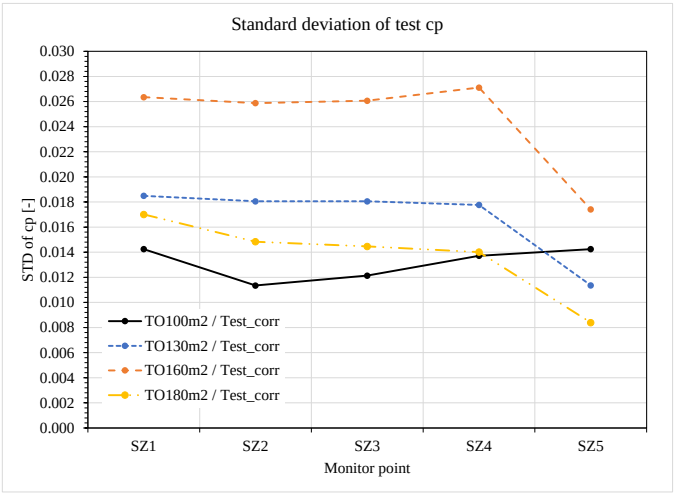

Fig. 22: Standard deviation of test static pressure coefficients of SZ1 to SZ5 for different flight cases

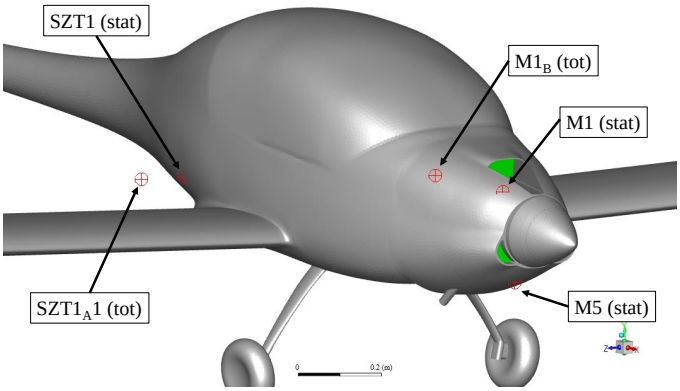

Fig. 23: Location of pressure probes SZT1, $SZT1_A1$, $M1_B$, M1 and M5

The variation of static and total pressures (p_s, p_t) relative to ambient static pressure will be shown using corrected measurement data. Note, that differences between actual and target flight speeds were insignificant.

In Fig. 24 Left the variation of p_s is depicted for probe M1. For both VT and CR flight conditions a good match between CFD and test data can be observed. Also, the effect of the propeller is clearly visible and captured by the applied VBM model. The maximum (max.) deviation between CFD and measured values is 23 Pa while the average (av.) is 11.3 Pa representing 11.2% and 5.5% deviation from the av. measured values, respectively.

From Fig. 24 Right one can conclude that the variation of p_t at $SZT1_A1$ probe shows a similarly good match between measurement and CFD with av. 49.3 Pa (5.1%) and max. 124 Pa (12.8%) deviation. The propeller down wash effect is clearly visible here as well. For VT case at the lowest flight-speed a significant drop in total pressure can be seen – indicating that the probe was operating in a sepation bubble – and this separation was captured by the CFD simulation. On the other hand, for

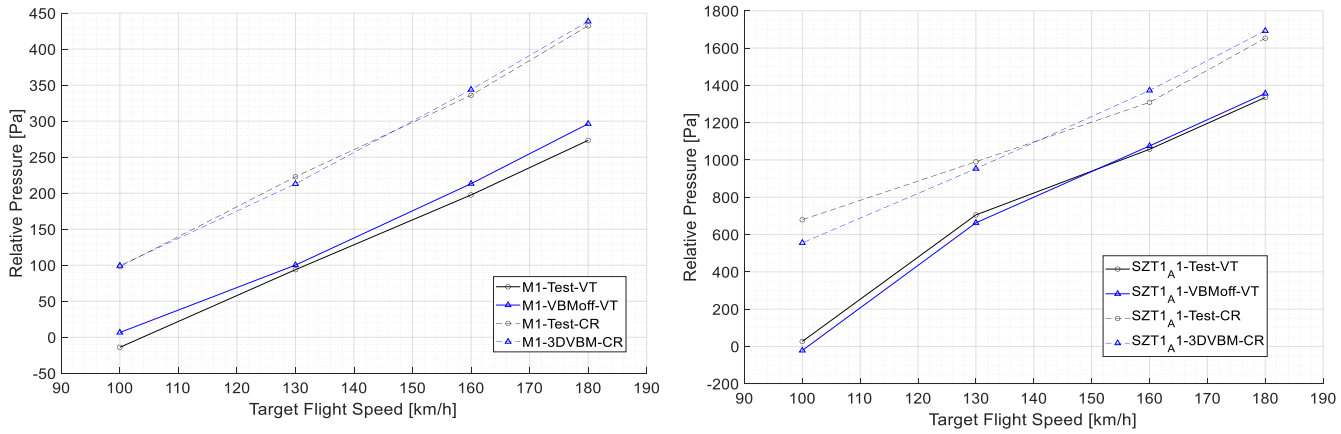

Fig. 24: Left: Variation of p_s at probe M1 for condition VT and CR. Right: Variation of p_t at probe SZT1$_A$1 for condition VT and CR

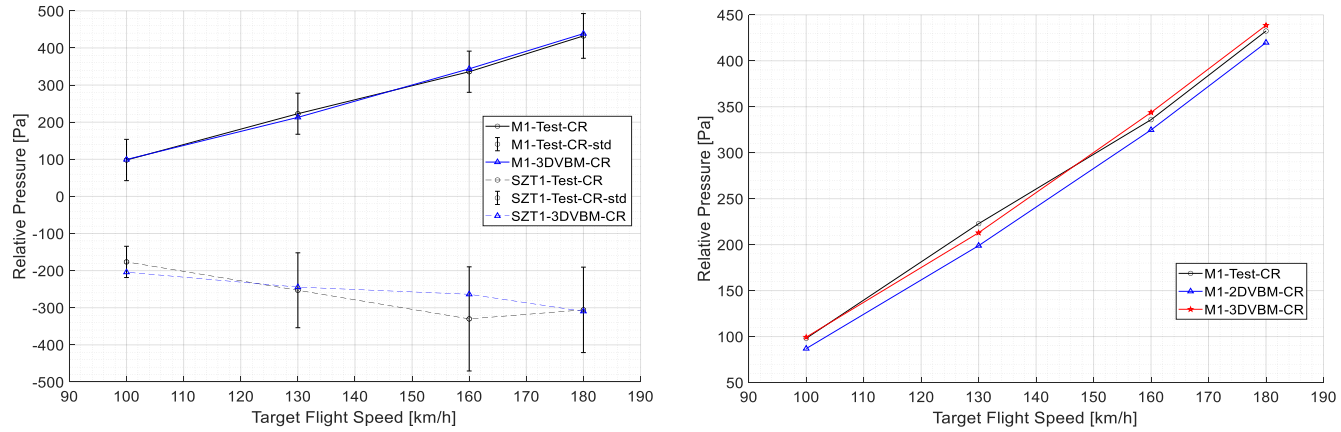

Fig. 25: Left: Variation of p_s at probe M1 and SZT1 at condition CR. Right: Variation of p_s at probe M1 for conditions CR with 2D- and 3D-VBM

the CR case this separation is surpressed by the increased momentum of the flow induced by the propeller; the CFD model with the applied VBM captures this phenomenon as well.
In Fig. 25 Left the variation of p_s is depicted at probes M1 and SZT1 for the cruise case. As it was expected the fluctuation of measured pressure at probe SZT1 is significantly higher compared to M1. The visualised error-bars show the standard deviation of the measured dataset: av. std. was 56.7 Pa and 99.6 Pa for M1 and SZT1, respectively. For SZT1 the max. difference of p_s from measurement is 66.3 Pa (24.9%) the av. is 26.6 Pa (10.0%). Note that the predicted accuracy of the measurement system is ±30 Pa. It can be seen from Fig. 25 Right that 3D-VBM improves the match with measurement compared to the 2D-VBM for M1 at cruise by reducing av. deviation from 14.7 Pa (5.4%) to 6.3 Pa (2.3%). However, this cannot be said for all probe positions; at many of them switching between 2D- and 3D-VBM resulted in no significant change.

4 Summary

A comprehensive study was carried out concerning the engine bay and the external aerodynamic assessment of a real motor-glider aircraft with the utilisation of 3D corrected VBM based on the work of Zipszer et al. (2022).
Engine bay intake and exit flow rates at different conditions were determined using a detailed CFD model. The sensitivity of the water cooler intake to AoA was explored, and a simplified model based on total pressure differences was proposed.
By comparing flight test data with CFD results the validity of the applied modelling approach was demonstrated. The effect of propeller downwash was clearly visible even further downstream from the propeller which proves the importance to account for propeller wake effects. Both 2D- and 3D-VBM results showed a good match with test data. 3D-VBM offers some improvements for the investigated cases; however, its superiority over 2D-VBM is observed mainly in the vicinity of the propeller plane.

Acknowledgment

This work was supported by the Hungarian Government through the NKFI Fund (grant number: 2018-1.2.2-KFI-2018-00057).

Tables

Tab. 1: Finalised baseline mesh settings

Location	Surface mesh type	Max. or Target mesh size [mm]	Min. mesh size [mm]	Curvature angle [deg]	Growth rate	Cells per gap
BOI	Body Of Influence	50	n/a	n/a	1.2	n/a
Gear rods and wheels	Curvature	20	4	8	1.2	n/a
Spinner	Curvature	20	3	8	1.2	n/a
Wing	Curvature	20	3	8	1.1	n/a
Tail	Curvature	20	6	8	1.1	n/a
Fuselage	Face Size	20	n/a	n/a	1.2	n/a
Wing trailing edge	Proximity	6	0.3	n/a	n/a	1

Tab. 2: Inflation-layer settings used for the different target y^+ values

Max. y^+ target	1^{st} layer thickness [mm]	Number of layers	Transition ratio	Growth rate	Total thickness [mm]
30	0.3	17	0.277	1.2	31.8
5	0.05	25	0.199	1.2	23.6
1	0.01	26	0.353	1.3	30.5

References

M. Balczó, I. Goricsán, T. Lajos, T. Régert, and P. Sebestyén. Prediction of wind load acting on telecommunication masts. In *IABSE Symposium*, volume 92(25), 2006.

M. Balland, O. Verseux, and M. J. Esteve. Aero thermal computations with experimental comparison applied to aircraft engine nacelle compartment. In *Proc. ASME Turbo Expo 2005: Power for Land, Sea, and Air*, volume 3, pages 1217–1225, 2005.

G. Buonomo, M. Musto, N. Bianco, G. Rotondo, G. Pezzella, and G. Mingione. Aerothermal analysis of an aircraft nacelle in the framework of a fully coupled approach. In *Italian Association of Aeronautics and Astronautics XXII Conference*, 2013.

P. Gula, D. Ulma, K. Zurek, and R. Zurawski. Challenges of turboprop engine installation on small aircraft. *Aircraft Engineering and Aerospace Technology*, 91(7):938–948, 2019.

A. C. Jackson and A. Vinegar. A technique for measuring frequency response of pressure, volume, and flow transducers. *J Appl Physiol Respir Environ Exerc Physiol*, 47(2):462–467, 1979.

P. Lapka, M. Seredynski, P. Furmanski, A. Dziubinski, and J. Banaszek. Simplified thermo-fluid model of engine cowling in small airplane. *Aircraft Engineering and Aerospace Technology*, 86(3):242–249, 2014.

P. Lapka, M. Bakker, P. Furmanski, and H. van Tongeren. Comparison of 1d and 3d thermal models of the nacelle ventilation system in a small airplane. *Aircraft Engineering and Aerospace Technology*, 90(1):114–125, 2018.

M. Mackay. Static pressure measurement with surface-mounted disc probes. *Experiments in Fluids*, 9(1-2):105–107, 1990.

A. Olejnik, A. Dziubinski, and L. Kiszkowiak. Cfd simulation of engine nacelle cooling on pusher configuration aircraft. *Aircraft Engineering and Aerospace Technology*, 93(9):1421–1429, 2021.

D. L. Pelley, D. Morris, and P. Richards. Aerodynamic force deduction on yacht sails using pressure and shape measurements in real time. In *4th High Performance Yacht Design Conference*, pages 28–37, 2012.

W. Stalewski and J. Zóltak. The preliminary design of the air-intake system and the nacelle in the small aircraft- engine integration process. *Aircraft Engineering and Aerospace Technology*, 86(3):250–258, 2014.

G. Zipszer, Sz. Varró, B. Darázs, M. Gyöngyösi, and Á. Horváth. Artificial intelligent enhanced virtual blade model. In *Proc. Conference on Modelling Fluid Flow (CMFF'22)*, pages CMFF22–029, 2022.